aerospace

MDPI

Article

A Turbulent Inflow Generation Method for the LES of High Re Flow by Scaling Low Re Flow Data

Lei Luo * and Honghu Ji

Aero-Engine Thermal Environment and Structure Key Laboratory of Ministry of Industry and Information Technology, Nanjing University of Aeronautics and Astronautics, Nanjing 210016, China
* Correspondence: cepeluolei@nuaa.edu.cn

Abstract: The rescaling–recycling method (RRM) is usually used to generate turbulent inflow for the LES of compressible wall-bounded flows, which can lead to relatively high computational cost for high Re flows since the mesh resolution increases exponentially with Re number. A turbulent inflow generation method based on the scaling of low Re flow, referred as TIG-LowRe, is proposed, aiming at reducing the computational cost when applying the RRM. To validate the proposed method, the TIG-LowRe method was applied to generate turbulent inflow for the LES of a non-isothermal round jet flow at Re = 86,000. Two cases were carried out with the inflow generated based on two round pipe flows at Re = 10,000 and 24,000. The results show that the mean and fluctuating temperatures of the two cases agree well with the experimental data. In the case of low Re flow at Re = 10,000, the jet flow decays too fast along the axial direction, the mean and fluctuating axial velocities are over-predicted and the radial fluctuating velocity is under-predicted. By increasing the Re of the low Re flow to 24,000, the decay rate of the jet flow decreases and the accuracies of the mean and fluctuating axial velocities are obviously improved, while the radial fluctuating velocity shifts further away from the experimental data. The main reason for the difference between the two cases is that more fine turbulent structure of the inflow in case-Re10000 is lost than in case-Re24000 during the turbulence generation process.

Keywords: turbulent inflow generation; LES; high Re flow; low Re flow

check for updates

Citation: Luo, L.; Ji, H. A Turbulent Inflow Generation Method for the LES of High Re Flow by Scaling Low Re Flow Data. *Aerospace* **2023**, *10*, 808. https://doi.org/10.3390/aerospace10090808

Academic Editor: Lawrence S. Ukeiley

Received: 14 March 2023
Revised: 7 June 2023
Accepted: 23 June 2023
Published: 15 September 2023

1. Introduction

Large eddy simulation (LES) is one of the most promising computational fluid dynamics (CFD) models to solve fluid flow problems, and it is now widely applied to simulate jet flows [1]. It is important to set turbulent inflows that are as realistic as possible for the LES of jet flows, since turbulent inflows that are not realistic enough greatly increase the calculation error, as proved by Salkhordeh and Kimber [2]. For high Re jet flows, the computational cost of turbulent inflow generation is a problem.

To set an ideal turbulent inflow is difficult because this requires that the inflow vary stochastically and continuously with space and time and also satisfy statistical turbulent characteristics in both the space domain and time domain, including the first and high-order moments, the spatial correlations, the spectrum distribution of turbulent kinetic energy and other related variables [3–5]. Various methods have been proposed to generate turbulent inflow, and these methods can be classified into three categories: the transition-inducing method, the synthetic turbulence generation method and the recycling method, according to Wu [5] and Dhamankar et al. [3].

In the transition-introducing method, the inlet is located in a place where the flow is laminar, so no or simple turbulence information is required at the inlet, but the domain between the inlet and the region of interest should be long enough such that the laminar flow can naturally evolve to a turbulent state. The transition of laminar-to-turbulent usually requires a very long evolving distance and thus leads to huge computational cost [6].

Introducing artificial disturbance can accelerate the generation of turbulence, which, however, should be carefully executed. Mild and reasonable disturbances can be eventually overwhelmed by the naturally evolving turbulence, but inappropriate disturbances can produce spurious fluctuations [7]. Moreover, even on the condition of being imposed with artificial disturbance, the computational cost of the transition-introducing method is still much larger than that of other methods, so it is now mainly limited to studying flow in the turbulent transition state.

The synthetic turbulence generation method artificially mimics turbulent eddies at the inlet based on known characteristics of the turbulent flow, so it avoids the need for a long transition domain to form turbulence. There are about five main strategies applied in the synthetic method [3]: the spectral-representation-based approach, the proper orthogonal decomposition (POD) approach, the digital filter approach, the volumetric-forcing-based approach and the synthetic eddy approach.

The spectral-representation-based approach decomposes fluctuations in turbulent flow into a summation of a series of Fourier harmonics, after which by controlling the amplitude, phase and frequency of the Fourier harmonics, turbulent inflow that satisfies specific turbulent length scale, time scale and energy spectrum can be generated [8]. The POD approach reconstructs the spatial distribution of the fluctuation in turbulent flow based on times series data that are usually obtained from experiments, and in the reconstruction process, only the main modes containing the largest possible energy are considered [9]. The digital filter approach designs digital filters to filter random signals to feature the specified spatial length scale and Reynolds stress tensor, and the digital filters are usually designed using empirical spectrum shape and correlation function [10]. The volumetric-forcing-based approach induces turbulent fluctuations via introducing artificial body force in the governing momentum equations over a designated domain near the inlet, and desired shear stress profiles are achieved on some inner planes of the domain by controlling the magnitude of the body force [11]. The synthetic eddy approach calculates velocity fluctuations based on a predesigned 2D or 3D fluctuating vorticity field that is controlled by predefined spatial and temporal functions [12]. Some synthetic methods may involve two or more approaches. Recently, Hao et al. [13] proposed a method that uses POD, digital filtering and mode decomposition to construct turbulent fluctuations based on specified Reynolds stress and random signal.

The major advantages of the synthetic method include that it requires only a short developing distance to form realistic turbulence and that it is able to generate turbulent inflow in arbitrary geometries. Therefore, the synthetic method has received much attention. Some synthetic methods have been developed in commercial CFD codes so that they can be used by engineers conveniently. For example, the Vortex method [14] and the Spectral Synthesizer [15] were developed in the general CFD code ANSYS Fluent. However, most of the synthetic methods only focus on the synthesis of velocity, which is not enough for compressible turbulent flows, because fluctuations in the thermodynamic variables, including temperature, density and pressure, are also important in the compressible condition.

The strategy of the recycling method is extracting instantaneous velocities continuously from a plane inside the calculation domain to the inlet so that the flow can develop continuously and generate turbulence eventually. Wu [5] classified the recycling method into the strong recycling method and the weak recycling method. In the strong recycling method, the strict periodic condition is applied, while in the weak recycling method, the data are recycled and then rescaled to satisfy specific statistics (e.g., mean velocity and Reynolds stresses) before being mapped back to the inlet, so the weak recycling method is also called the recycling–rescaling method (RRM).

The RRM was originally proposed by Lund and Wu [16] for spatially developing incompressible boundary layers. In Lund's method, the instantaneous velocity is decomposed into mean and fluctuation, the boundary layer is divided into inner and outer layers, and then the mean velocity and fluctuation velocity are separately recycled and rescaled in each layer. Spalart et al. [17], Uzun et al. [18] and Baha-Ahmadi et al. [19] proposed a simpler RRM by directly recycling the instantaneous velocity or only recycling the fluctuating velocity in the entire boundary layer. Urbin et al. [20] and Stolz et al. [21] began to extend Lund's RRM to compressible turbulent boundary layers by recycling and rescaling density and temperature along with velocity. Xu et al. [22] proposed another version of RRM for compressible flows in which the temperature was related to the velocity based on Morkovin's hypothesis. The validity of the RRM they proposed for compressible flows has been proven by many works and is widely used for compressible flows [23,24].

The RRM requires an extra domain with the same shape as the inlet to execute the recycling process. The computational cost of the extra domain is acceptable for low Re jet flows, while for high Re jet flows, the cost is huge. Taking the round jet flow as an example, if the turbulent inflow is generated in an extra pipe domain with a length of $5D$ (where D is the pipe diameter) that is discretized by a typical resolution for LES, i.e., $\Delta x^+ \approx 50$, $\Delta z^+ \approx 20$, $\Delta y^+_{\text{min}} < 1$ [25], the total grid number of the extra domain is about 0.6 million for $\text{Re} = 10^4$, and the numbers increase to about 8 million and 30 million for $\text{Re} = 5 \times 10^4$ and 10^5, respectively. For most industrial flows, the grid number is usually on the order of ten million, which means that for high Re jet flows, the cost of generating turbulent inflow would be too computationally intensive compared with the overall cost.

The way to reduce the extra cost when applying the RRM is reducing either the length or the grid number of the extra domain. However, the length of the extra domain should not be too short, as "spurious periodicity" would be introduced into the inflow during the recycling process, as proved by Nikitin [26]. As for reducing the grid number, this would lead to low resolution, which increases the simulation error significantly. Considering that the grid number is proportional to the flow Re number, a new method of generating turbulent inflow for high Re jet flows based on turbulence data of lower Re flows is proposed for the purpose of decreasing computational cost. For narrative purposes, the new method is referred to as the TIG-LowRe method (Turbulent Inflow Generation based on Low Re flow).

In this paper, the TIG-LowRe method is used to generate turbulent inflow for the LES of a non-isothermal round jet flow at Re = 86,000, and the simulation results are compared with experimental data to validate the TIG-LowRe. The rest of the paper is arranged as follows. Section 1 introduces the details of the TIG-LowRe method; Section 2 describes the numerical details; Section 3 analyzes the simulation results; and Section 4 presents the conclusions.

2. Turbulent Inflow Generation Based on Low Re Flow

The instantaneous velocity is composed of the mean and the fluctuation:

$$u_i(x, y, z, t) = U_i(x, y, z) + u_i'(x, y, z, t) \tag{1}$$

where u_i is the velocity; the lower-case and upper-case characters represent the instantaneous and the mean variable, respectively, and the one with apostrophe represents the fluctuation; the subscript $i = 1, 2, 3$ denotes the streamwise, wall-normal and spanwise coordinates x, y, z, respectively; and t is time.

The strategy of the TIG-LowRe method is setting the profiles of the mean velocities as constant at the inlet while generating the fluctuating velocities based on an extra flow that is at much lower Re. Figure 1 takes the pipe flow as an example to sketch the method. As sketched in Figure 1, in order to generate turbulent inflow for a flow at Re_h (the high Re flow and also the main flow), firstly a turbulent flow at a lower Re number, Re_l (the low Re flow), is simulated; then, fluctuating velocities on an interior plane of the low Re flow (low Re data plane) are extracted out and scaled to obtain fluctuating velocities for the high Re flow; finally the fluctuating components are added to the mean components to obtain the instantaneous velocities of the high Re flow. Two conditions are assumed in the TIG-LowRe method, one of which is that both the low Re flow and the high Re flow are turbulent, while the other is that the low Re data plane and the inlet of the high Re flow are geometrically similar.

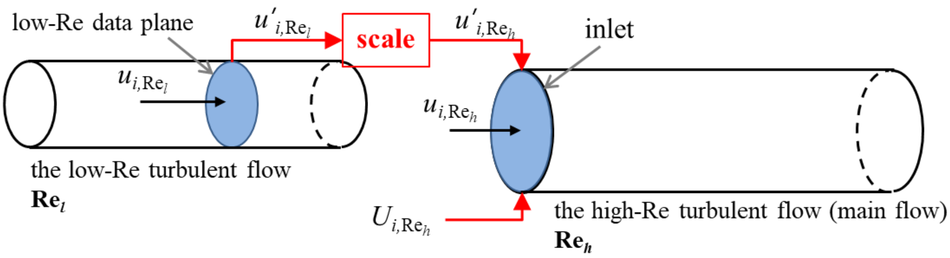

Figure 1. Schematic of the TIG-LowRe method.

According to Figure 1, the fluctuating velocities of the high Re flow are calculated as:

$$u'_{i,\mathrm{Re}_h}\left(x_{\mathrm{Re}_h}, y_{\mathrm{Re}_h}, z_{\mathrm{Re}_h}, t\right) = u'_{i,rms,\mathrm{Re}_h}\left(x_{\mathrm{Re}_h}, y_{\mathrm{Re}_h}, z_{\mathrm{Re}_h}\right)\frac{u'_{i,\mathrm{Re}_l}\left(x_{\mathrm{Re}_l}, y_{\mathrm{Re}_l}, z_{\mathrm{Re}_l}, t\right)}{u'_{i,rms,\mathrm{Re}_l}\left(x_{\mathrm{Re}_l}, y_{\mathrm{Re}_l}, z_{\mathrm{Re}_l}\right)} \quad (2)$$

where the subscript "*rms*" means the root mean square (RMS) sampled over time, and the subscripts "Re_l" and "Re_h" represent the low Re flow and the high Re flow, respectively. Similar scaling techniques as Equation (2) are applied by some RRM methods without involving Re changes [18,27].

In the TIG-LowRe method, the U_i in Equation (1) and the u'_{i,rms,Re_h} in Equation (2) should be set in advance, which can be obtained from published research in the literature and experimental data. In conditions where no data are available, the target data can be calculated using the RSM (Reynolds stress model).

The data of flows at Re_l and Re_h are different on both the space and time scales. To map the low Re data to the inlet of the high Re flow, the low Re data plane must be scaled to fit the inlet of the high Re flow. In the RRM, the dimensionless wall unit y^+ is usually used to map the recycling data to the inlet [16]. However, it is inappropriate to scale the space with y^+ in the TIG-LowRe method, since the ranges of y^+ between the low Re flow and the high Re flow are quite different. Therefore, the dimensional coordinates are used to scale the low Re data plane:

$$u'_{i,\mathrm{Re}_l}\left(x_{\mathrm{Re}_l}, y_{\mathrm{Re}_l}, z_{\mathrm{Re}_l}, t\right) \xrightarrow[z_{\mathrm{Re}_h}=a\cdot z_{\mathrm{Re}_l}]{\substack{x_{\mathrm{Re}_h}=a\cdot x_{\mathrm{Re}_l} \\ y_{\mathrm{Re}_h}=a\cdot y_{\mathrm{Re}_l}}} u'_{i,\mathrm{Re}_l}\left(x_{\mathrm{Re}_h}, y_{\mathrm{Re}_h}, z_{\mathrm{Re}_h}, t\right) \quad (3)$$

where a is the ratio of the inlet geometrical size of the high Re flow to that of the low Re data plane. Therefore,

$$u'_{i,\mathrm{Re}_h}\left(x_{\mathrm{Re}_h}, y_{\mathrm{Re}_h}, z_{\mathrm{Re}_h}, t\right) = \frac{u'_{i,rms,\mathrm{Re}_h}\left(x_{\mathrm{Re}_h}, y_{\mathrm{Re}_h}, z_{\mathrm{Re}_h}\right)}{u'_{i,rms,\mathrm{Re}_l}\left(x_{\mathrm{Re}_h}, y_{\mathrm{Re}_h}, z_{\mathrm{Re}_h}\right)} u'_{i,\mathrm{Re}_l}\left(x_{\mathrm{Re}_h}, y_{\mathrm{Re}_h}, z_{\mathrm{Re}_h}, t\right) \quad (4)$$

As for the time scale, the rule to follow is:

$$\frac{\Delta t_{\mathrm{Re}_l, sample}}{t_{\mathrm{Re}_l}} \approx or > \frac{\Delta t_{\mathrm{Re}_h, time\,step}}{t_{\mathrm{Re}_h}} \quad (5)$$

where $\Delta t_{\mathrm{Re}_l, time\,step}$ is the time interval of extracting data from the low Re data plane; $\Delta t_{\mathrm{Re}_h, time\,step}$ is the time step applied to simulate the high Re flow; and t_{Re_l} and t_{Re_h} are the turbulent integral timescales of the low Re flow and the high Re flow, respectively. The application of Equation (5) is to avoid introducing too strong of a temporal correlation to the high Re flow.

3. Numerical Methodology

To validate the TIG-LowRe, LES simulations of the non-isothermal round jet flow measured by Xu et al. [28] with the turbulent inflow generated by the TIG-LowRe method were carried out. The jet flow is sketched in Figure 2. As shown in the figure, the cylindrical coordinates are used to describe the jet flow, and x, r, φ are the axial, radial and circumferential coordinates, respectively. The Re number of the jet flow based on the pipe diameter D and average axial velocity at the pipe exit U_j is 86,000. The temperature of the air in the pipe is uniform at 313 K. The temperature and pressure of the ambient air are constant at 301 K and 101,325 Pa, respectively. The pipe length is long enough so that the flow is fully developed before being ejected into the air.

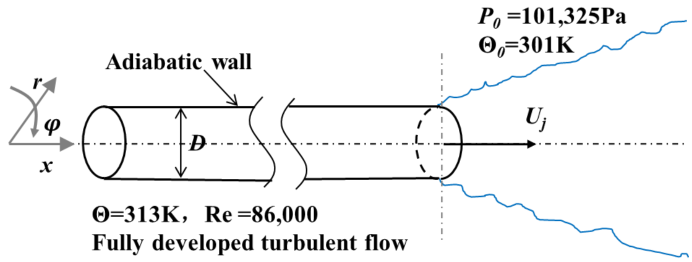

Figure 2. Schematic of the jet flow.

Two LES cases were carried out, and the Re numbers of the low Re flows used to generate turbulent inflow were 10,000 and 24,000 for the two cases. For narrative purposes, these respective two cases are referred as case-Re10000 and case-Re24000.

3.1. Governing Equations

Considering that the density variation of the jet flow is small, the incompressible solver was used. The filtered governing equations for incompressible flows in Cartesian coordinates are:

$$\frac{\partial \overline{u}_j}{\partial x_j} = 0 \tag{6}$$

$$\frac{\partial \rho \overline{u}_i}{\partial t} + \frac{\partial \rho \overline{u}_i \overline{u}_j}{\partial x_j} = -\frac{\partial \overline{p}}{\partial x_i} + \frac{\partial \sigma_{ij}}{\partial x_j} - \frac{\partial \tau_{ij}}{\partial x_j} \tag{7}$$

$$\frac{\partial \rho \overline{h}}{\partial t} + \frac{\partial \rho \overline{h} \overline{u}_j}{\partial x_j} = \frac{\partial \overline{p}}{\partial t} + \widetilde{u}_j \frac{\partial \overline{p}}{\partial x_j} + \frac{\partial}{\partial x_j}\left(\lambda \frac{\partial \overline{\Theta}}{\partial x_j}\right) - \frac{\partial \rho}{\partial x_j}\left(\overline{hu_j} - \overline{h}\overline{u}_j\right) \tag{8}$$

where the overbar represents the filtered (or resolved) value; $\overline{u}$, $\overline{p}$, $\overline{h}$, $\overline{\Theta}$ are the filtered velocity, pressure, sensible enthalpy and temperature, respectively; λ is the thermal conductivity; σ_{ij} is the stress tensor due to molecular viscosity; μ is the molecular viscosity; and τ_{ij} is the subgrid-scale stress defined by Equation (9), which is modeled by the subgrid model developed by Nicoud and Ducros [29].

$$\tau_{ij} = \rho\left(\overline{u_i u_j} - \overline{u}_i \overline{u}_j\right) \tag{9}$$

The last term on the right hand of Equation (8) is the subgrid enthalpy flux, estimated as:

$$\rho\left(\overline{hu_j} - \overline{h}\overline{u}_j\right) = -\frac{\mu_{SGS} c_p}{\mathrm{Pr}_{SGS}} \frac{\partial \overline{\Theta}}{\partial x_j} \tag{10}$$

For the sake of narration, the overbar is not shown in the following sections.

3.2. Details of the LES of the Non-Isotherm Round Jet Flow

The simulation domain is a cylinder with a diameter of 20D and a length of 16D, as shown by Figure 3. The axial domain is from $x = -1D$ to 15D, and the pipe exit is located at $x = 0D$. A 0.5D long geometry of the pipe is included in the domain. The domain is meshed by hexahedral grids using the O-Block approach. Taking the grid settings of the LES of a round jet flow at Re $= 10^5$ executed by Kim [30] as reference, the distribution of grid numbers was set as 360 × 100 × 135, corresponding to the axial, circumferential and radial directions, respectively. The area inside the red box is the key area of jet flow developing, which occupies 88% of the mesh. The circumferential grid is equispaced, while the axial grid spacing Δx and the radial grid spacing Δr increase along the axial and radial directions, respectively. Figure 4 shows the distribution of Δx along the center line and Δr at location $x/D = 0, 5, 10, 14$. The figure shows that the smallest mesh is in the wall vicinity at the pipe exit, where Δx is about $0.018D$ and Δr is about $0.003D$, and the largest mesh in the red box is near $x/D = 15$, $r/D = 6$, where Δx is about $0.095D$ and Δr about $0.08D$.

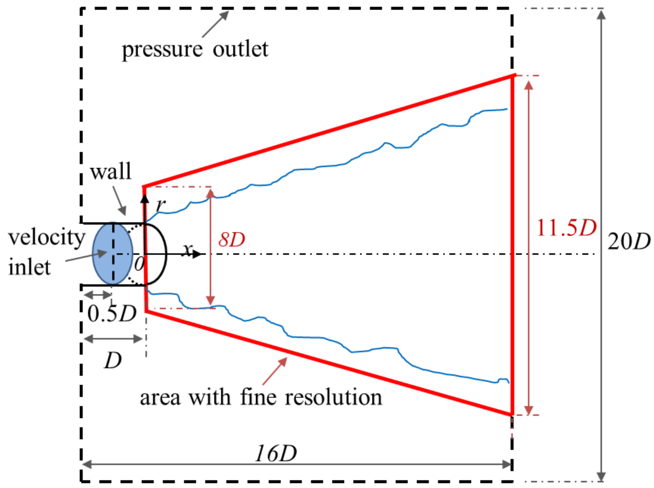

Figure 3. Simulation domain of the LES of jet flow.

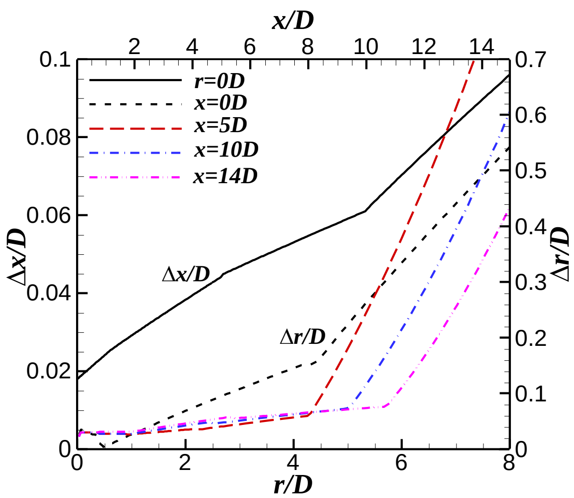

Figure 4. Mesh size in axial and radial directions.

The commercial CFD code Fluent was used to execute the simulations. The pressure-based solver was chosen to solve the equations. The TIG-LowRe method was executed through the Scheme commands of Fluent. The solution methods were set according to the advice of Menter [31]. The second-order central difference scheme and bounded central difference scheme were used for the spatial discretization of momentum and the energy equations, respectively. The scheme adopted for time discretization was the second-order implicit, non-iterative time advancement. The second-order scheme was used for pressure interpolation. The least-squares cell-based scheme was selected for gradient calculation.

The inlet of the simulation domain was set as the velocity inlet. The inlet temperature was assumed to be constant and was set as 313 K. The inlet velocity was generated by the TIG-LowRe method, so the mean velocity and the root mean square of the fluctuating velocity of the main flow were provided as target data as shown by Equations (1) and (4).

The target data and the low Re flow data were calculated using the RSM and the LES, respectively, and related calculation details are described in the next sub-section.

The outlet of the simulation domain was set as the pressure outlet, and a constant pressure of 101,325 Pa and a constant temperature of 301 K were set at the outlet. The pipe wall was set as adiabatic with no slip wall condition. The flow field was initialized with a velocity of 0 m/s, temperature of 301 K and pressure of 101,325 Pa.

The time step was set as $0.01D/U_j$ to make the maximum CFL number less than 1.0. After running for about $60D/U_j$, the convergence of the simulations was reached because the net mass flux of the inflow and the outflow decreased to be less than 0.04% of the total inflow mass flux and the variables of the flow fields were statistically steady. After running for another $40D/U_j$, the sampling process began and lasted for more than $330D/U_j$, and the time-averaged statistics were averaged circumferentially so as to improve the statistical convergence.

3.3. Generating Turbulent Inflow for the LES of the Jet Flow

3.3.1. Calculation of the Target Data

A pipe flow at Re = 86,000 was simulated via the RSM using Fluent to provide the target data, i.e., the mean velocities and the root mean square of the velocity fluctuations, for the TIG-LowRe method. The simulation domain was a pipe with a diameter of D and a length of $5D$. The domain was meshed by about 0.68 million hexahedral grids. The grids were uniformly distributed in the axial and circumferential directions, while in the radial direction, the grid spacing decreased towards the wall, and the dimensionless spacing Δy^+ of the first layer near the wall was about 1.

The inlet and the outlet of the domain were coupled by a strict periodic condition. The temperature of the air in the pipe was 313 K. The wall was set as adiabatic with the no-slip wall condition. After the RSM simulation was completed, the mean velocities and corresponding Reynolds stresses on the middle cross-section of the pipe were extracted out as the target data for the TIG-LowRe method.

3.3.2. Calculation of the Low Re Data

Two pipe flows at Re = 10,000 and Re = 24,000, respectively, were simulated via the LES using Fluent to provide low Re data for the TIG-LowRe method. The simulation domain was a pipe with a length-to-diameter ratio of 5. Hexahedral grids were used to mesh the domain, and the total grids of the Re = 10,000 case and the Re = 24,000 case were about 0.72 million and 1.9 million, respectively. For both cases, the wall–normal grid spacing Δy^+ was about 0.4~0.5 near the wall and about 15~20 near the pipe center, the axial grid spacing Δx^+ was about 32~35, and the circumferential grid spacing $r\Delta\varphi^+$ was less than 15.

The boundary conditions of the two low Re flow cases were set in the same way as the RSM case, and the solution method settings were the same as the LES of the jet flow above. The time steps were about $0.0018FTT$(flow through time) for the Re = 10,000 case and $0.00026FTT$ for the Re = 24,000 case so that the maximum CFL numbers of both cases were about 0.5.

The two low Re flow simulations reached statistical steadiness after 5~7 FTT, and then the fluctuations in the axial, radial and circumferential velocities of the middle cross-section of the pipe were extracted out and saved as the low Re data for the TIG-LowRe method.

4. Results and Analysis

4.1. Velocity Fluctuations at the Inlet of the LES of the Jet Flow

The mean velocities at the inlets of case-Re10000 and case-Re24000 were set directly using the target mean velocities, while the velocity fluctuations were generated by the TIG-LowRe method. Figure 5 shows the radial profiles of the normalized fluctuating velocities, in which the ${u'_{rms}}^+$, ${v'_{rms}}^+$, ${w'_{rms}}^+$ represent the dimensionless root mean squares of the axial, radial and circumferential fluctuating velocities, respectively. The figure shows that the fluctuating velocities in the three directions generated by the TIG-LowRe method agree well with the target data in most regions, but they shift away from the target data in the near wall region. Considering that the Re of the low Re flow is much lower than the Re of the jet flow, it is reasonable to expect shifts in the process of mapping the low Re data to the inlet of the jet flow.

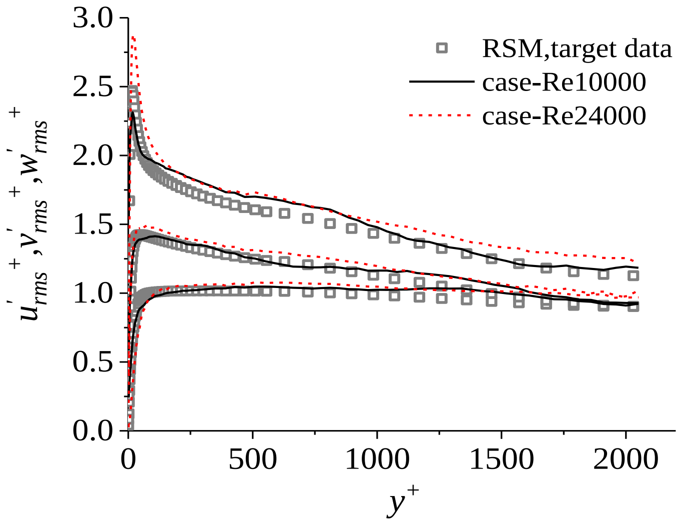

Figure 5. Radial profiles of the RMS of normalized fluctuating axial, circumferential and radial velocities of the inflow generated by the TIG-LowRe.

4.2. Mean Axial Velocity and Temperature

The simulation results were validated with the experimental data of Xu [28]. Figure 6 shows the dimensionless mean axial velocities and temperatures along the jet flow centerlines of case-Re10000 and case-Re24000, and Figure 7 shows the radial profiles of the mean axial velocities at location $x/D = 3$. In the figures, Θ is the mean temperature and θ' is the fluctuating temperature; the subscript "*j*" represents taking the average over the pipe exit, and the subscript "*c*" represents the variable on the jet flow centerline; the superscript "*" represents the temperature relative to the mean temperature of the ambient air, for example, $\Theta^* = \Theta - \Theta_0$.

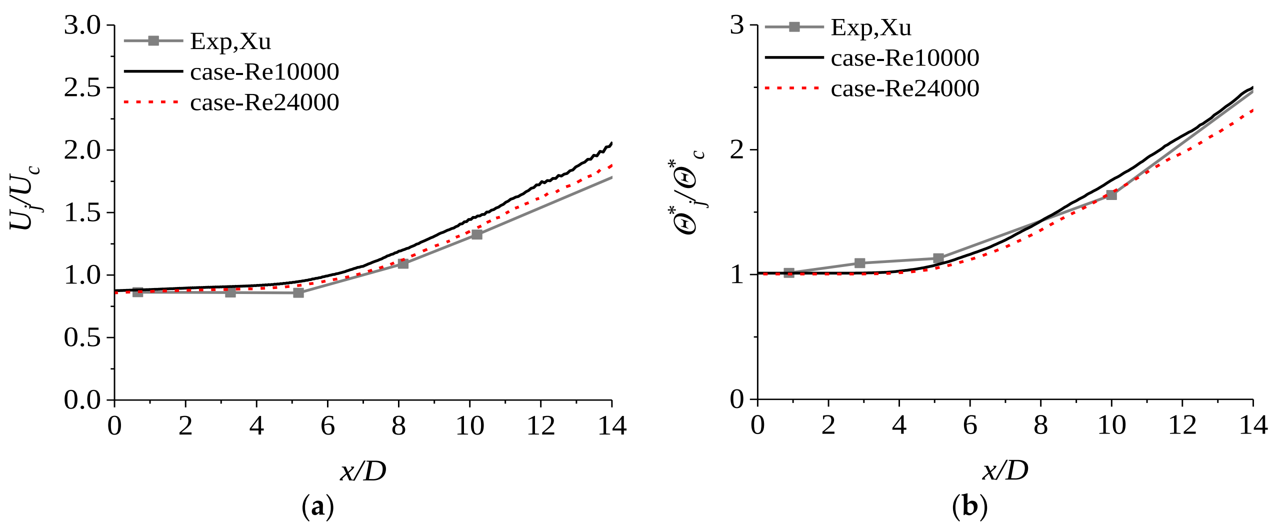

Figure 6. Distributions on the jet flow centerline of the normalized (**a**) mean axial velocity and (**b**) mean temperature.

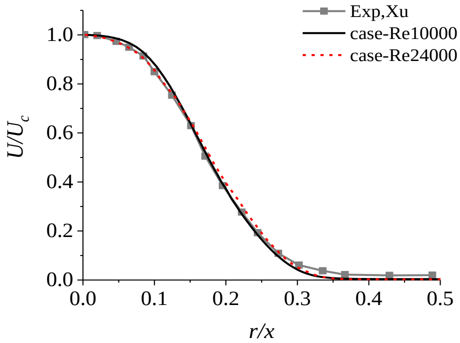

Figure 7. Radial profiles of the normalized mean axial velocity at x/D = 3.

As shown in Figure 6, the dimensionless mean velocity and temperature of case-Re10000 grow faster than that of case-Re10000 on the centerline, which means the jet flow of case-Re10000 attenuates quicker in the axial direction than case-Re24000. The jet flow core lengths of both cases are about 6D, which are consistent with the experimental data. In the core region, the mean velocities and temperatures of both cases are close to the experimental data. Beyond the core region, case-Re10000 overpredicts the mean velocity, and the error is about 10.7% at $x/D = 10$. In contrast, the mean velocity of case-Re24000 is closer to the experimental data, and the corresponding error decreases to about 3.8%. For the mean temperature, both cases are close to the experimental data, although case-Re24000 is underpredicted by about 5% in the far end of the jet flow. In the radial direction, the distributions of the mean axial velocities of both cases agree well with the experimental data.

4.3. Fluctuating Velocities and Temperature

Figure 8 presents the distributions of dimensionless fluctuations of axial velocity, radial velocity and temperature along the jet flow centerline. It can be seen from the figures that the fluctuations of case-Re10000 are larger than those of case-Re24000 in the initial and middle sections of the jet flow. As the jet flow develops, the fluctuations of case-Re24000 increase faster and become closer to those of case-Re10000 in the rear section of the jet flow.

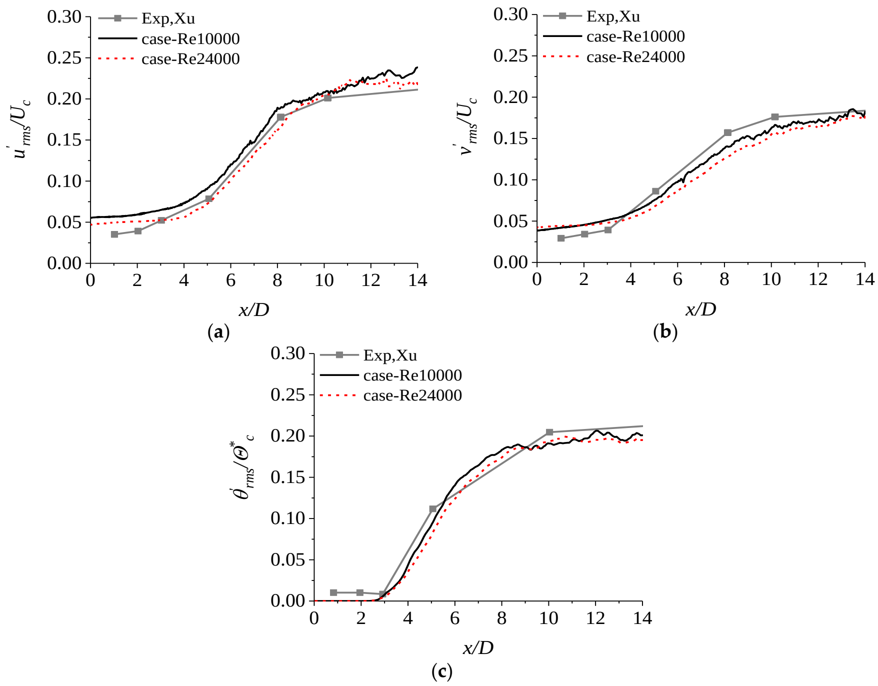

Figure 8. Distributions on the jet flow centerline of the normalized fluctuations of the (**a**) axial velocity; (**b**) radial velocity; and (**c**) temperature.

In the region of $x/D < 3$, the fluctuating variables of both cases deviate from the experimental data obviously. This region is close to the inlet of the simulation domain where the flow is largely affected by the inflow turbulence, so the deviations in this region mean that the inflow fluctuating velocities at the inlet are overly large and the inflow fluctuating temperature is overly small. However, it can be seen from Figure 5 that the inflow fluctuating velocities match well with the target data in the pipe central area, so the deviations in the near inlet region should be attributed to the differences between the target data and the experimental data; this kind of calculation error could be removed by using target data closer to the experimental data.

In the region of $x/D > 3$, case-Re10000 over-predicts the axial fluctuating velocity, especially in the rear area of the jet flow, where the error is about 7%~10%. By contrast, the axial fluctuating velocity of case-Re24000 is closer to the experiment, and the error in the rear area of the jet flow decreases to about 3%~7%. The two cases under-predict the radial fluctuating velocity, but case-Re10000 demonstrates better agreement with the experiment. The error in the radial fluctuating velocity at $x/D = 10$ is about 6% for case-Re10000 and about 11% for case-Re24000. For the fluctuating temperature, the agreement of both cases with the experimental data is comparable, and the errors at $x/D = 10$ are about 5% for both cases.

Figure 9a–c show the radial profiles of the dimensionless fluctuations of axial velocity, radial velocity and temperature, respectively, at location $x/D = 3$. In the two cases, the axial fluctuating velocities are over-predicted in most regions, but the locations of the peak values are consistent with the experiment. The axial fluctuating velocity of case-Re10000 deviates more from the experiment than that of case-Re24000, and at the peak value location, the errors are about 24% for case-Re10000 and about 10% for case-Re24000. The fluctuating radial velocities of the two cases are closer to the experimental data than the fluctuating axial velocities, but the locations of peak value deviate radially outward from the experimental data by about 0.05 D and 0.08 D for case-Re10000 and case-Re24000, respectively. For the fluctuating temperature, the two cases agree very well with the experimental data in both value and shape of profile.

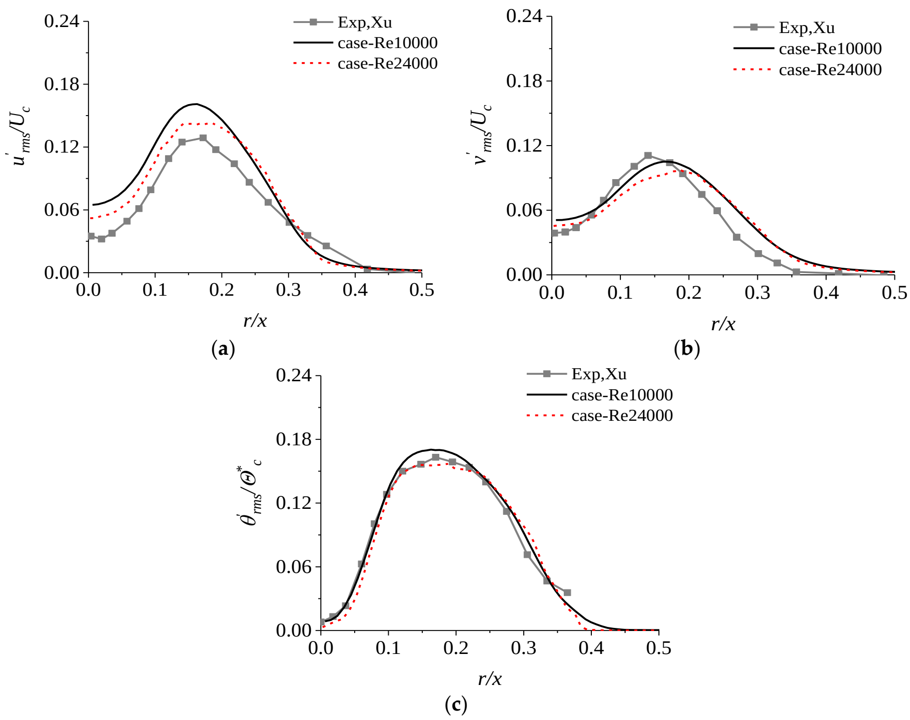

Figure 9. Radial profiles at *x/D* = 3 of the normalized fluctuating: (**a**) axial velocity; (**b**) radial velocity; and (**c**) temperature.

According to Figures 6–9, the distribution profiles of velocities and temperatures of both case-Re10000 and case-Re24000 are similar to the experiment, although there are some differences between the simulation values and the experimental data. Case-Re24000 presents better agreement with the experiment in the distributions of mean velocity, axial fluctuating velocity than case-Re10000, but it performs poorer than case-Re10000 in predicting the radial fluctuating velocity. In terms of the mean temperature and fluctuating temperature, both cases show good agreement with the experiment.

4.4. Turbulent Structures

The turbulent structure of the jet flow was visualized in the form of the instantaneous iso-surfaces of the Q criterion, as shown in Figure 10. It can be seen that the vortex is small inside the pipe, and it grows immediately after the flow runs out of the pipe because of Kelvin–Helmholtz instability. Inside the pipe, the vortex of case-Re10000 is distributed more sparsely than that of case-Re24000, which results in a sparser vortex in the vicinity of the pipe exit, but in the area further away from the pipe exit, the vortex of case-Re10000 becomes larger compared to that of case-Re24000.

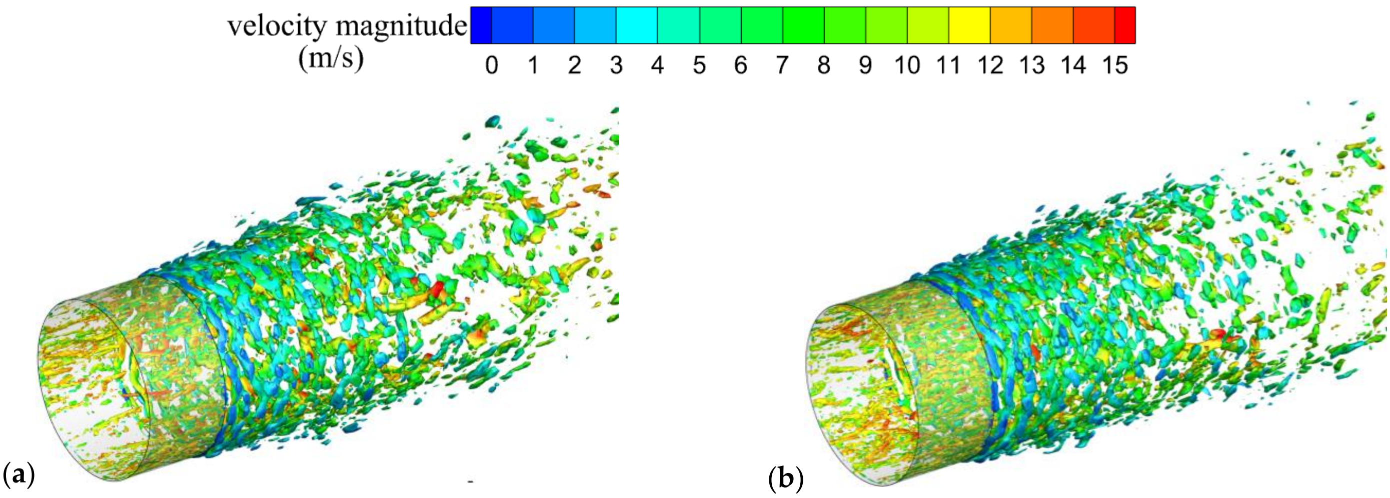

Figure 10. Turbulent structure of the jet flow in the form of the instantaneous iso-surfaces of the Q criterion (**a**) case-Re10000 and (**b**) case-Re24000.

Figure 11 shows the contour lines of the vorticity magnitude on the pipe exit plane and the symmetry plane. The figure shows that the vorticity iso-line on the pipe exit of case-Re24000 is finer than that of case-Re10000, especially in the region away from the pipe wall. The difference exists until the flow runs out of the pipe, and the vorticity in the central region of case-Re10000 remains smaller than case-Re24000 for the initial developing stage of the jet flow, as shown by the symmetry plane.

According to Figures 10 and 11, case-Re24000 presents a better resolution of the fine turbulence structures for the initial stage of the jet flow, which is expected since the Re of the flow providing turbulent inflow for case-Re10000 is smaller than that for case-Re24000. This means that case-Re10000 has smaller inflow fluctuation than case-Re24000. McMullan's work about the turbulent mixing layer [32] proved that when two parallel flows mix, reducing the fluctuation of the mixing flows would lead to an increase in the mixing rate and larger turbulent fluctuation. Therefore, the vortex of case-Re10000 becomes larger than that of case-Re24000 as the jet flow develops, and this is also the reason that the jet flow of case-Re10000 attenuates faster than that of case-Re24000, as shown in Figure 6.

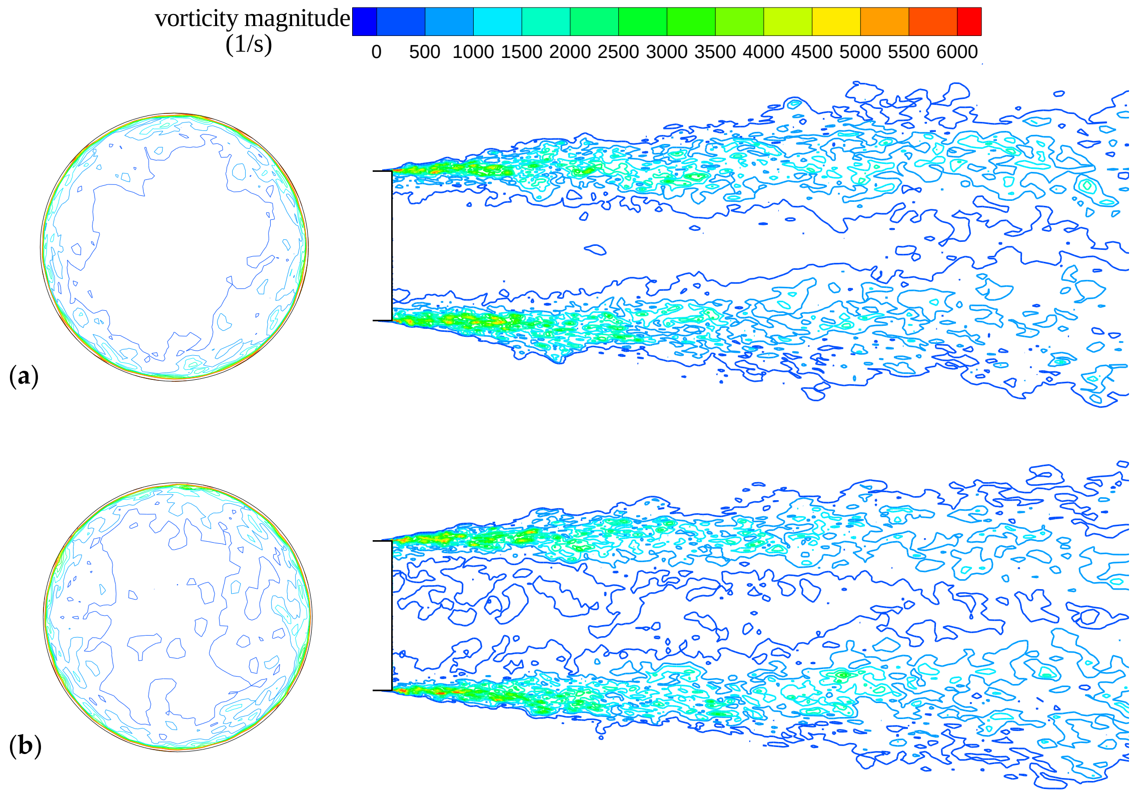

Figure 11. Iso-lines of the instantaneous vorticity magnitudes of (**a**) case-Re10000 and (**b**) case-Re24000.

5. Conclusions

Motivated by reducing the high computational cost of generating turbulent inflow for high Re jet flows using the recycling–rescaling method, a turbulent inflow generation method based on Low Re flow, TIG-LowRe for short, is proposed. To validate the TIG-LowRe method, two LES simulation cases of a non-isothermal round jet flow at Re = 86,000 were carried out, and the turbulent inlet velocities of the two cases were generated by the TIG-LowRe method based on round pipe flows at Re = 10,000 and Re = 24,000.

The simulation results show that when the turbulent inflow of the jet flow is generated by the flow at Re = 10,000, the mean temperature and fluctuating temperature agree well with the experiment, but the velocities shift away from the experimental data by some extent; as a result, the mean axial velocity decays too fast along the axial direction, the axial fluctuating velocity is over-predicted and the radial fluctuating velocity is under-predicted. By increasing the Re number of the low Re flow to 24,000, the decay rates of the axial mean velocity and the velocity fluctuations decrease, which improves the agreements of the axial mean velocity and fluctuating velocity with the experiment but increases the difference between the radial fluctuating velocity and the experiment. Meanwhile, the good agreement of the mean temperature and fluctuating temperature with the experiment is retained. The analysis of the turbulent structure proves that when the inflow is generated by the flow at Re = 10,000, more fine turbulent structure is lost than for that generated by the flow at Re = 24,000, which makes the jet flow mix with the ambient fluid more quickly so that larger fluctuations are generated.

In summary, the distributions of the velocity and temperature of the jet flows with turbulence generated by the TIG-LowRe method are similar to those of the experiment, so it can be concluded that the TIG-LowRe method is able to generate realistic turbulent inflow for jet flows, with the exception that the fine turbulent structure of the main flow is lost because of the Re difference between the low Re flow and the main flow, which increases the simulation error. However, by increasing the Re of the low Re flow properly, finer turbulent structure can be provided in the inflow, and the simulation error can be reduced while the computer cost remains affordable.

Furthermore, though the TIG-LowRe method cannot be used in compressible flows, its validity is proven in this paper, and its feasibility for compressible flows will be studied in the author's future work.

Author Contributions: Conceptualization, L.L.; methodology, L.L.; software, L.L.; validation, L.L. and H.J.; formal analysis, L.L. and H.J.; investigation, L.L. and H.J.; writing—original draft preparation, L.L.; writing—review and editing, L.L. and H.J.; supervision, H.J. All authors have read and agreed to the published version of the manuscript.

Funding: This research received no external funding.

Data Availability Statement: The data presented in this study are available on request from the corresponding author.

Conflicts of Interest: The authors declare no conflict of interest.

References

1. Yang, Z. Large-Eddy Simulation: Past, Present and the Future. *Chin. J. Acoust.* **2015**, *28*, 11–24.
2. Salkhordeh, S.; Kimber, M.L. Full-Field Dependence on Inlet Modeling of Non-Isothermal Turbulent Jets Using Validated Large Eddy Simulations. *J. Fluids Eng.* **2019**, *141*, 81401–81408. [CrossRef]
3. Dhamankar, N.S.; Blaisdell, G.A.; Lyrintzis, A.S. Overview of Turbulent Inflow Boundary Conditions for Large-Eddy Simulations. *AIAA J.* **2017**, *56*, 1–18.
4. Tabor, G.R.; Baba-Ahmadi, M.H. Inlet Conditions for Large Eddy Simulation: A Review. *Comput. Fluids* **2010**, *39*, 553–567. [CrossRef]
5. Wu, X. Inflow Turbulence Generation Methods. *Annu. Rev. Fluid Mech.* **2017**, *49*, 23–49. [CrossRef]
6. Sayadi, T.; Hamman, C.W.; Moin, P. Direct Numerical Simulation of Complete H-Type and K-Type Transitions with Implications for the Dynamics of Turbulent Boundary Layers. *J. Fluid Mech.* **2013**, *724*, 480–509. [CrossRef]
7. Martha, C. Toward High-Fidelity Subsonic Jet Noise Prediction Using Petascale Supercomputers. Ph.D. Thesis, Purdue University, West Lafayette, IN, USA, 2012.
8. Castro, H.G.; Paz, R.R. A Time and Space Correlated Turbulence Synthesis Method for Large Eddy Simulations. *J. Comput. Phys.* **2013**, *235*, 742–763. [CrossRef]
9. Druault, P.; Lardeau, S.; Bonnet, J.-P.; Coiffet, F.; Delville, J.; Lamballais, E.; Largeau, J.-F.; Perret, L. Generation of Three-Dimensional Turbulent Inlet Conditions for Large-Eddy Simulation. *AIAA J.* **2004**, *42*, 447–456. [CrossRef]
10. Xie, Z.; Castro, I. Efficient Generation of Inflow Conditions for Large Eddy Simulation of Street-Scale Flows. *Flow Turbul. Combust.* **2008**, *81*, 449–470. [CrossRef]
11. Spille-Kohoff, A.; Kaltenbach, H.J. Generation of Turbulent Inflow Data with a Prescribed Shear-Stress Profile. In Proceedings of the 3rd AFOSR International Conference on DNS/LES in DNS/LES Progress and Challenges, Arlington, TX, USA, 5–8 August 2001.
12. Benhamadouche, S.; Jarrin, N.; Addad, Y.; Laurence, D. Synthetic Turbulent Inflow Conditions Based on a Vortex Method for Large-Eddy Simulation. *Prog. Comput. Fluid Dyn.* **2006**, *6*, 50–57. [CrossRef]
13. Hao, M.; Hope-Collins, J.; Mare, L. Generation of Turbulent Inflow Data from Realistic Approximations of the Covariance Tensor. *Phys. Fluids* **2022**, *34*, 115140. [CrossRef]
14. Mathey, F.; Cokljat, D.; Bertoglio, J.P.; Sergent, E. Specification of LES Inlet Boundary Condition Using Vortex Method. In Proceedings of the 4th International Symposium on Turbulence, Heat and Mass Transfer, Antalya, Turkey, 12–17 October 2003.
15. Smirnov, A.; Celik, I.; Shi, S. Random Flow Generation Technique for Large Eddy Simulations and Particle-Dynamics Modeling. *J. Fluids Eng.* **2001**, *123*, 359–371. [CrossRef]
16. Lund, T.S.; Wu, X.; Squires, K.D. Generation of Turbulent Inflow Data for Spatially-Developing Boundary Layer Simulations. *J. Comput. Phys.* **1998**, *140*, 233–258. [CrossRef]
17. Sparlat, P.R.; Strelets, M.; Travin, A. Direct Numerical Simulation of Large-Eddy-Break-Up Devices in a Boundary Layer. *Int. J. Heat Fluid Flow* **2006**, *27*, 902–910.
18. Uzun, A.; Hussaini, M.Y. On Some Issues in Large-Eddy Simulations for Chevron Nozzle Jet Flows. In Proceedings of the 49th AIAA Aerospace Sciences Meeting including the New Horizons Forum and Aerospace Exposition, Orlando, FL, USA, 4–7 January 2011.
19. Baha-Ahmadi, M.H.; Tabor, G. Inlet Conditions for LES Using Mapping and Feedback control. *Comput. Fluids* **2009**, *38*, 1299–1311. [CrossRef]
20. Urbin, G.; Knight, D. Large-eddy simulation of a supersonic boundary layer using an unstructured grid. *AIAA J.* **2011**, *39*, 1288–1295. [CrossRef]
21. Stolz, S.; Adams, N.A. *LES of Supersonic Boundary Layers Using the Approximate Deconvolution Model, Direct and Large Eddy Simulation IV*; Kluwer Academic: Norwell, MA, USA, 2001; pp. 269–276.

22. Xu, S.; Martin, M.P. Assessment of inflow boundary conditions for compressible turbulent boundary layers. *Phys. Fluids* **2004**, *16*, 2623–2639. [CrossRef]
23. Helm, C.M.; Martin, M.P. Large eddy simulation of two separated hypersonic shock/turbulent boundary layer interactions. *Phys. Rev. Fluids* **2022**, *7*, 074601. [CrossRef]
24. Zuo, F.; Memmolo, A.; Huang, G.; Pirozzoli, S. Direct numerical simulation of conical shock wave–turbulent boundary layer interaction. *J. Fluids Mech.* **2019**, *877*, 167–195. [CrossRef]
25. Davidson, L. Large Eddy Simulations: How to Evaluate Resolution. *Int. J. Heat Fluid Flow* **2009**, *30*, 1016–1025. [CrossRef]
26. Nikitin, N. Spatial Periodicity of Spatially Evolving Turbulent Flow Caused by Inflow Boundary Condition. *Phys. Fluids* **2007**, *19*, 302–314. [CrossRef]
27. Luo, L.; Ji, H. Turbulent Inlet Temperature Generation for Undeveloped Pipe Flow with Simple Recycling-Rescaling Methods. *AIAA J.* **2019**, *57*, 3094–3099. [CrossRef]
28. Xu, G.; Antonia, R.A. Effect of Initial Conditions on the Temperature Field of a Turbulent Round Free Jet. *Int. Commun. Heat Mass Transf.* **2002**, *29*, 1057–1068. [CrossRef]
29. Nicould, F.; Ducros, F. Subgrid-Scale Stress Modelling Based on the Square of the Velocity Gradient Tensor Flow. *Turbul. Combust.* **1999**, *62*, 183–200. [CrossRef]
30. Kim, J.; Choi, H. Large eddy simulation of a circular jet: Effect of inflow conditions on the near field. *J. Fluid Mech.* **2009**, *620*, 383–411. [CrossRef]
31. Menter, F.R. *Best Practice: Scale-Resolving Simulation in ANSYS CFD*; ANSYS Germany GmbH: Darmstadt, Germany, 2015.
32. McMullan, W.A. The Effect of Boundary Layer Fluctuations on the Streamwise Vortex Structure in Simulated Plane Turbulent Mixing Layers. *Int. J. Heat Fluid Flow* **2017**, *68*, 87–101. [CrossRef]